(Received 14 March 2024, Accepted 17 April 2024, Scheduled 6 May 2024)

Research on the Grounding Grid Electrical Impedance Imaging Algorithm Based on Improved Tikhonov and Lp Regularization

Lele He[1,*], Lei Yang[2], Xiaoheng Yan[1], Weihua Chen[1], and Shangfei Huang[1]

[1] *Faculty of Electrical and Control Engineering, Liaoning Technical University, China*
[2] *State Grid Ningxia Electric Power Co Ltd, Zhongwei Power Supply Company, China*

ABSTRACT: In this paper, an improved hybrid regularized grounded network imaging algorithm (ITR-Lp) combining Tikhonov regularization and Lp regularization is proposed; through the improvement of the filtering function, the correction of small magnitude for large singular values and increasing magnitude of correction with decreasing singular values for small singular values is implemented for the improvement of the convergence of the solution. The proposed algorithm constructs a regularization matrix to achieve selective correction of singular values and improve the convergence of the solution, while Lp regularization is used to enhance the sparsity of the solution and improve the boundary contrast. the effect of node distribution on convergence is investigated, and finally the ITR-Lp algorithm is validated by simulation and experiment. The results show that the ITR-Lp algorithm proposed in this paper achieves the lowest resistivity relative errors of 0.1695 and 0.1089 for resistive networks with 1 corrosion and 2 corrosions, respectively. The method has good convergence and boundary contrast, which effectively improves the pathology of the inverse problem of imaging the electrical impedance tomography of grounding grid.

1. INTRODUCTION

The grounding grid is an important part of substations and power plants, and the normal operation of the grounding grid is a prerequisite for the protection of personnel and equipment [1]. Because the grounding grid is located in a special working environment, it is easy to be corroded and thus cannot work properly [2], so it needs to be tested regularly to ensure its normal and stable operation [3, 4]. Due to the complex electromagnetic environment in the actual environment, it is difficult to obtain accurate results by the currently used diagnostic methods [5], and in practice, for the detection of corrosion of the grounding grid, after the power outage, the grounding grid will be dug out to observe the corrosion situation.

The Electrical Impedance Tomography (EIT) technique, as an advanced visualization tool, is noninvasive, low cost, easy to operate, and has fast response [6, 7], and it is widely used in medical inspection and industrial inspection. Scholars were inspired by the application of medical and industrial inspection to apply the EIT technique to grounding grid detection, Wang et al. [8] proposed a magnetic source excitation detection method to determine corrosion breakpoints by magnetic field signals. Liu et al. [9] proposed a magnetic detection technique for electrical impedance imaging of grounding grids. However, the electromagnetic field is insensitive to changes in corrosion, and the complex electromagnetic environment of substation leads to inaccurate magnetic field signals. Yang et al. [10] proposed a method to detect grounding grid corrosion by measuring voltage, and Li et al. [11] proposed a voltage measurement-based electrical impedance tomography technique and improved the ill-conditioned of inverse problem using Tikhonov regularization. Chen et al. [12] proposed to improve Tikhonov by changing the regularization matrix to improve the stability of the solution and accuracy, but the image over-smoothing problem occurs during reconstruction using Tikhonov regularization [13, 14]. To solve the problem of excessive smoothing of Tikhonov regularization, scholars proposed Lp $(1 \leq p \leq 2)$ regularization based on L1 and L2 to increase the edge contrast and improve the imaging quality. Estatico et al. [15] applied Lp regularization to microwave imaging and showed that the imaging effect of Lp regularization is better than L2 regularization. Zhang et al. [16] demonstrated that Lp regularization had the advantage of avoiding excessive smoothing of the reconstructed image compared to L2 regularization. Liu et al. [17] applied Lp regularization to image reconstruction, and the results proved that Lp regularization can improve spatial resolution. Li et al. [18] proposed an adaptive weighting algorithm to solve the problem of Lp regularization parameter selection, and Zhu [19] applied Lp regularization to image denoising and proved that Lp regularization can maintain image contrast and prevent step effect.

Therefore, in order to mitigate the ill-conditioning inherent in the grounding grid resistance inverse problem, enhance solution stability, and address the issue of image smoothing, this study proposes a hybrid regularization algorithm based on an improved Tikhonov and Lp approach. Firstly, two distinct models of the grounding grid inverse problem are formulated for imaging experiments: one based on priori topological information and the other on unknown topological information. Subsequently, utilizing the grounding grid model with known topological information, varying levels of noise are introduced

* Corresponding author: Lele He (1416169662@qq.com).

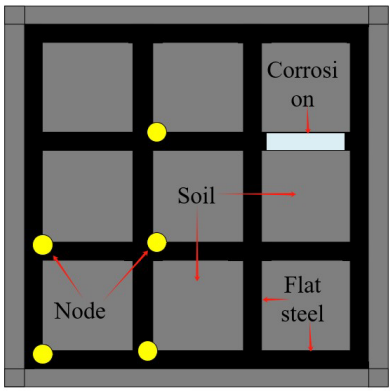

FIGURE 1. Measurement model for the forward problem of grounding grid.

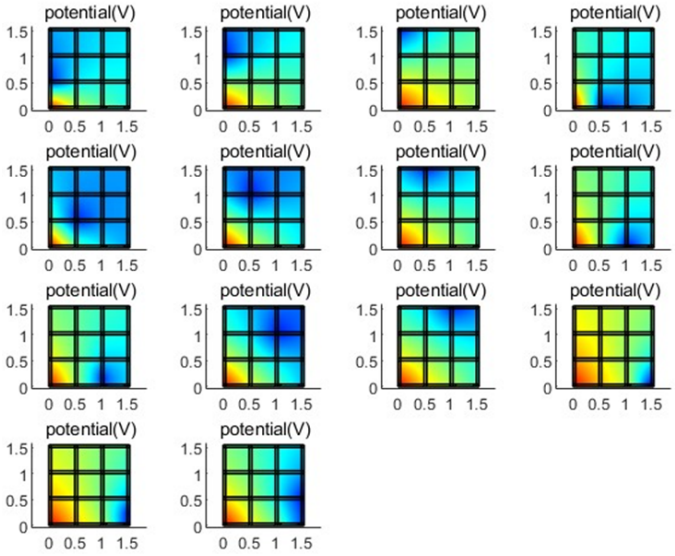

FIGURE 2. Voltage distribution map of grounding grid forward problem.

into the measurement data to assess the algorithm's robustness to noise. The effectiveness of the algorithm is further verified by experiments.

2. PRINCIPLE OF GROUNDING GRID ELECTRICAL IMPEDANCE IMAGING

The essence of grounding grid impedance is to inject current into the grounding grid, measure the voltage on the flat steel, reconstruct the distribution of grounding grid resistivity based on current and voltage, determine the location of corrosion based on resistivity distribution, and σ represents the distribution of conductivity in the flat steel. Assuming that the boundary electrodes are perfectly conductive, current is then applied through these electrodes to obtain internal potential u. The mathematical model can be described as follows:

$$\nabla \cdot (\sigma \nabla u) = 0, ..., u \in \Omega \tag{1}$$

σ represents the distribution of conductivity, and u denotes the voltage. In this assumed model, satisfying the static excitation condition and absence of current sources, the boundary conditions can be described as follows:

$$u + z_l \sigma \nabla u \cdot \vec{e} = v_l, ..., u \in \partial\Omega \tag{2}$$

$$\int \sigma \nabla u \cdot \vec{e} = I_l, ..., u = \partial\Omega \tag{3}$$

where z_l represents the measured resistance between electrodes. v_l represents the measured voltage at the electrode. $\partial\Omega$ represents the boundary of the solution domain. $\vec{e}$ is the normal vector to the boundary. I_l represents the injected current at the jth electrode. l represents the number of electrodes.

The inverse problem of grounding grid electrical impedance tomography imaging can be considered as the process of solving the distribution of resistivity from the relationship between calculated voltage and measured voltage, as expressed in Equation (4)

$$U(\rho) = V \tag{4}$$

$U(\rho)$ represents the voltage obtained within the target area after applying excitation current I, computed using the finite element method [20, 21]. V denotes the measured voltage acquired through the measurement electrodes. Due to the presence of errors, it is challenging for the computed voltage $U(\rho)$ to exactly match the measured voltage V. Therefore, this problem can be addressed using the method of least squares. By subtracting the computed voltage $U(\rho)$ from the measured voltage V, an error function is obtained, which is used to solve for the resistivity distribution of the grounding grid.

$$F(\rho) = \frac{1}{2} ||U(\rho) - V||_2^2 \tag{5}$$

Due to the severe ill-conditioning of the grounding grid inverse problem, the solution will eventually fail in the process of iterative solution. Therefore, in order to improve the ill-conditioning of the inverse problem, the most common method is to use the regularization method [22], which adds penalty terms to the error function for constraint and reduces the condition number of the Jacobian matrix to make the solution process of the inverse problem more stable [23].

2.1. Grounding Grid Simulation Model

The simulation model for the forward problem of the grounding grid is crucial for obtaining the measured voltage data. Since grounding grids are typically grid-like structures, this study constructs 2D models of a 3×3 grid and a 4×3 grid using COMSOL software. The forward problem measurement model of the 3×3 grid is shown in Fig. 1, comprising flat steel, corrosion, and soil. The black areas represent flat steel with a conductivity of 6×10^6 S/m; the white areas represent corrosion with a conductivity of 1×10^6 S/m; the gray areas represent

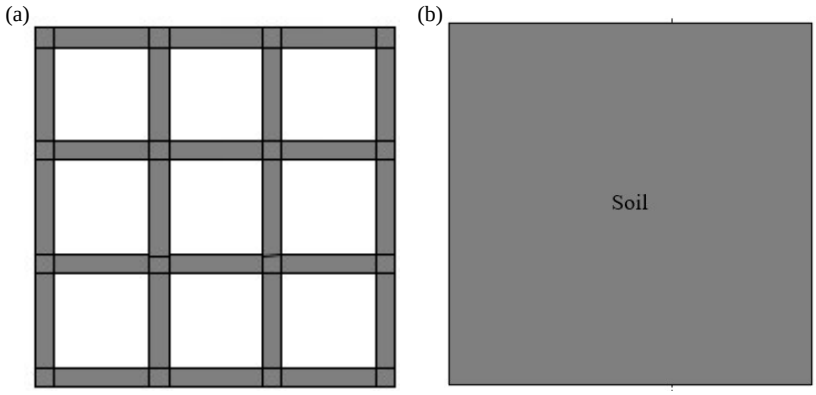

FIGURE 3. Inverse problem model of grounding grid. (a) Model with known topology structure. (b) Model with unknown topology structure.

soil with a conductivity of 0.005 S/m; the yellow areas denote measurement nodes, totaling 16 in this study.

The paper randomly selects 16 points as voltage data collection points in the model and injects 1 A of direct current into the grounding grid using a loop measurement method. Specifically, the 16th electrode point serves as the reference node. The injection nodes are determined by pairs such as $1 \sim 2$, $1 \sim 3, ..., 1 \sim 15$; $2 \sim 3$, $2 \sim 4, ..., 2 \sim 14, ..., 14 \sim 15$, with the former representing the injection node and the latter representing the current outflow node. This process yields a total of 105×13 measured voltage data points. In the combined simulation using COMSOL and MATLAB, node 1 serves as the measurement node. By stimulating the system according to pairs such as $1 \sim 2$, $1 \sim 3, ..., 1 \sim 15$, the corresponding potential distribution for each of these 14 stimulation methods can be obtained, as shown in Fig. 2. By analyzing the potential distribution, the voltage at the 16 measurement nodes under these 14 stimulation methods can be determined.

The grounding grid inverse problem model is adopted to obtain the resistivity ρ. In substations, the topology information of the grounding grid is usually documented in drawings. However, in some substations, this information may be lacking due to lost drawings. To address these two scenarios, this paper conducts simulation studies by constructing two different grounding grid models: one with a known topology structure and the other with an unknown topology structure. In the known topology structure, only the flat steel part is present, while in the unknown topology structure, only the soil part exists. Fig. 3 shows the grounding grid inverse problem models for both the known and unknown topology structures.

3. SOLVING THE ILL CONDITIONED PROBLEM OF GROUNDING GRID

3.1. Improved Tikhonov Regularization Method

The Tikhonov regularization method is a commonly used method for solving inverse problems, and its essence is to apply a damping effect to the objective function to achieve improvement of the solution process, and the strength of the damping effect is achieved through the regulation of the regularization parameters. The error function constructed by the Tikhonov regularization is obtained by adding the penalty function to Eq. (5)

$$F(\rho) = \frac{1}{2} ||U(\rho) - V| |_2^2 + \frac{1}{2} \alpha ||L(\rho - \rho_0)| |_2^2 \quad (6)$$

where L is the regularization matrix, which is generally the identity matrix, and α is the regularization parameter, which is generally $0 < \alpha < 1$. The original resistivity distribution ρ_0 can be calculated via the following formulas [24].

$$\rho^0 = (\rho_1, \rho_2, ..., \rho_N)^T = cL = c \begin{pmatrix} 1, 1 & \cdots & 1 \end{pmatrix}^T \quad (7)$$

$$c = \frac{\sum_{i=1}^{m} \sum_{j=1}^{n} (V_{ij} U_{ij} (L))}{\sum_{i=1}^{m} \sum_{j=1}^{n} (U_{ij} (L))^2} \quad (8)$$

Using Gaussian Newton iterative method to solve Equation (6) and Decomposition of Jacobian matrix J by singular value decomposition, the resistivity ρ is obtained as [25]

$$\rho^{k+1} = \sum_{i=1}^{m} \frac{\gamma_i^2}{\gamma_i^2 + \alpha} \frac{u_i^T}{\gamma_i} v_i \cdot (U(\rho^k) - V), \quad i = 1, 2, ..., m \quad (9)$$

where the standard Tikhonov's filter function is $f_i = \gamma_i^2 / (\gamma_i^2 + \alpha)$, and m is the number of non-zero eigenvalues. In Equation (8), $\gamma_1 > \gamma_2 > ... > \gamma_m$ is the non-zero eigenvalue in the singular value decomposition of the Jacobian matrix J. The filter function shows that the standard Tikhonov regularization uses a uniform correction magnitude for all singular values to suppress the effect of noise, but the uniform correction leads to a decrease in the accuracy of the solution, and in practice, the correction should be made according to the different sizes of the singular values.

Therefore, we proposed a regularization matrix to achieve selective correction of singular values, with small corrections to greater singular values and focused corrections to minor singular values. First, a singular threshold value γ_t was selected to classify all singular values. First $t - 1$ singular values were larger singular values, and the later $m - t + 1$ singular values

were smaller singular values. As the order of magnitude difference between the singular values in the Jacobi matrix is too large, a 3×3 grid grounding network was adopted as an example. The order of magnitude difference between the singular values of its Jacobi matrix was 10^{14}. The larger singular values correspond to positions in the regularization matrix which were set to 1 to reduce the impact of large singular value on the regularization results, thus better balancing the contribution of the regularization terms. The corresponding positions for the small singular values in the regularization matrix was set to $\sqrt[4]{\gamma_t/\gamma_r}$ for the same purpose. To avoid the large order of magnitude of elements in the regularization matrix, the constructed diagonal matrix of regularization can be expressed as follows [12, 13]:

$$H = \begin{bmatrix} 1 & 0 & 0 & 0 & 0 & 0 \\ 0 & 1 & 0 & 0 & 0 & 0 \\ \vdots & \vdots & \vdots & \vdots & \vdots & \vdots \\ 0 & 0 & \cdots & \sqrt[4]{\gamma_t/\gamma_r} & 0 & 0 \\ 0 & 0 & 0 & 0 & \ddots & 0 \\ 0 & 0 & 0 & 0 & 0 & \sqrt[4]{\gamma_t/\gamma_m} \end{bmatrix} \tag{10}$$

When the regularization matrix is the constructed diagonal matrix above, the filtering function can be segmentally expressed as

$$f = \begin{cases} \frac{\gamma_i^2}{\gamma_i^2+\alpha} \ldots 1 \le i \le t \\ \frac{\gamma_i^2}{\gamma_i^2+\alpha\sqrt[4]{\frac{\gamma_t}{\gamma_i}}} \ldots t < i \le m \end{cases} \tag{11}$$

From the filter function, it can be seen that for large singular values, only small amplitude corrections are made, and for small singular values, as i gets smaller, γ_t/γ_i gradually increases. The corrections for small singular values are gradually strengthened to achieve different amplitude corrections according to the size of γ_t.

The threshold singular value γ_t is chosen by using the condition number method. The condition number C is a commonly used metric to measure the ill-conditioning of matrix, if it satisfies

$$\left(\frac{\gamma_1}{\gamma_t}\right)^2 < C < \left(\frac{\gamma_1}{\gamma_{t+1}}\right)^2 \tag{12}$$

then the threshold singular value γ_t is determined.

The Tikhonov regularization using the two-parametric number of the solution as the penalty term leads to a smoothing effect of the solved solution, which in turn leads to an overly smooth imaged map and unclear boundary contrast.

3.2. Lp Regularization

Lp regularization, as a sparse regularization method, is proposed on the basis of L1 regularization and L2 regularization. L1 parametrization as a regularization term has high noise immunity and edge retention, and the reconstructed map of L2 parametrization will have an over-smooth effect; based on this, Lp regularization is proposed, where the range of p values is $1 \le p \le 2$ [26–28]. Choosing a suitable p value can ensure that the derived regularization solution has a large sparsity, suppresses the smoothing effect of Tikhonov regularization, and improves the boundary contrast. The error function constructed by the Lp regularization is added to Equation (5)

$$F(\rho) = \frac{1}{2}\left|\left|U(\rho) - V\right|\right|_2^2 + \lambda \left|\left|\rho\right|\right|_p^p \tag{13}$$

where λ is the regularization factor, and $x_p = \left(\sum_{j=1}^{n} |x_j|^p\right)^{\frac{1}{p}}$ is the p-norm of the solution.

When Eq. (13) is solved by Gaussian Newton's algorithm, Eq. (13) is unable to solve its differential when $p = 1$, so it is necessary to approximate Eq. (13), and the approximate objective function obtained can be expressed as Eq. (14) [29, 30]

$$F(\rho) = \frac{1}{2}\left|\left|U(\rho) - V\right|\right|_2^2 + \lambda \sum_{i=1}^{n} \left(\sqrt{\rho_i^2 + \beta}\right)^p \tag{14}$$

where $\beta > 0$ is a tiny adjustable constant.

3.3. Improved Tikhonov-Lp Regularization Algorithm

Based on the above analysis, this paper proposes a new error function, which uses a combination of improved Tikhonov and Lp regularization in the penalty function, denoted as ITR-Lp, to convert the inverse problem of grounding grid electrical impedance tomography imaging into an optimization problem, and uses a Gauss-Newton iterative algorithm in the solution method to solve the optimized error function and obtain a stable solution, based on the improved Tikhonov-Lp hybrid regularization of the error function as

$$\begin{aligned} F(\rho) &= \frac{1}{2}\left|\left|U(\rho) - V\right|\right|_2^2 + \frac{1}{2}\alpha\left|\left|H(\rho - \rho_0)\right|\right|_2^2 \\ &\quad + \lambda \sum_{i=1}^{n} \left(\sqrt{\rho_i^2 + \beta}\right)^p \end{aligned} \tag{15}$$

To solve the minimum of Eq. (12) by Gaussian-Newton iteration, we acquire the gradient vector of Eq. (12) via the Hessian matrix substituted into the framework of Newton-Gaussian iteration

$$\rho^{k+1} = \rho^k - \left[\nabla^2 F(\rho)\right]^{-1} \nabla F(\rho) \tag{16}$$

Let $F(\rho)$ find the first-order derivative of the resistivity ρ and make its first-order derivative equal to 0 to obtain the gradient vector of the error function

$$\begin{aligned} E(\rho) &= J^T(U(\rho) - V) + \alpha H^T \cdot H(\rho - \rho_0) \\ &\quad + \lambda \operatorname{diag}\left(p\left(\sqrt{\rho_i^2 + \beta}\right)^{p-2}\right)\rho \end{aligned} \tag{17}$$

Then let the gradient vector $E(\rho)$ of $F(\rho)$ find the first order derivative with respect to the resistivity ρ to obtain the Hessian matrix ignoring the higher order terms

$$E'(\rho) = J^T \cdot J + \alpha H^T \cdot H$$

TABLE 1. ITR-Lp based regularized grounded grid imaging algorithm.

Algorithm: ITR-Lp based regularized grounded grid imaging algorithm
Input: Jacobian matrix J, measurement voltage V, initial conductivity ρ_0
Initialization: regularization parameters α, λ, p, voltage error t, precision e.
Step 1: Decompose the Jacobian matrix $\boldsymbol{J}$ and construct the $\boldsymbol{H}$ matrix.
Step 2: Execute iteration when t > e
① Calculate the voltage $\boldsymbol{U}(\boldsymbol{\rho})$ from the conductivity solution
② Solve for the new resistivity ρ^{k+1} according to equation (16).
③ Solve for the voltage error t and determine whether t<e holds
Step 3: Output the solved resistivity ρ^{k+1}

$$+\lambda \operatorname{diag}\left(p\left(\sqrt{\rho_i^2+\beta}\right)^{p-2}\right) \tag{18}$$

Finally, the solution formula for the resistivity is obtained by substituting the obtained gradient vector $E(\rho)$ with the Hessian matrix $E'(\rho)$ into the Gaussian Newton iteration formula

$$\rho^{k+1}=\rho^k-\frac{\begin{array}{c}J^T(U(\rho)-V)+\alpha H^T\cdot H(\rho-\rho_0)\\+\lambda \operatorname{diag}\left(p\left(\sqrt{\rho_i^2+\beta}\right)^{p-2}\right)\rho\end{array}}{J^T\cdot J+\alpha H^T\cdot H+\lambda \operatorname{diag}\left(p\left(\sqrt{\rho_i^2+\beta}\right)^{p-2}\right)} \tag{19}$$

A pseudo-code implementation of the proposed algorithm for EIT image reconstruction is provided in Table 1.

3.4. Calculation of the Jacobi Matrix

In the grounding grid EIT inverse problem, J denotes the relationship between voltage change between electrodes and resistivity change, i.e., the potential change value induced by the resistivity change. The computed Jacobi matrix J_k can be expressed as follows when the kth excitation is input [31].

$$J_k=\begin{bmatrix}\frac{\partial U_1}{\partial \rho_1} & \frac{\partial U_1}{\partial \rho_2} & \cdots & \frac{\partial U_1}{\partial \rho_m}\\ \frac{\partial U_2}{\partial \rho_1} & \frac{\partial U_2}{\partial \rho_2} & \cdots & \frac{\partial U_2}{\partial \rho_m}\\ \vdots & \vdots & \cdots & \vdots\\ \frac{\partial U_L}{\partial \rho_1} & \frac{\partial U_L}{\partial \rho_2} & \cdots & \frac{\partial U_L}{\partial \rho_m}\end{bmatrix} \tag{20}$$

where L is the number of electrodes measured, and m is the number of profiling units. Multiple injections are generally required to increase the amount of information to ensure the success of the reconstruction, and if the number of independent injections is S, S such matrices together form the entire Jacobi matrix J, $J=[J_1,J_2,...,J_t,...,J_S]^T$.

The most common method Jacobi matrix calculation in grounding grid EIT is the difference method, which calculates as follows

$$J=\frac{\partial U}{\partial \rho}\approx\frac{U(\rho+\Delta\rho)-U(\rho)}{\Delta\rho}=\frac{\Delta U}{\Delta\rho} \tag{21}$$

The method needs to calculate the positive problem for once to obtain each column of the Jacobi matrix, and the entire matrix will need $S\times(m+1)$ times of positive problem calculation, and the positive problem calculation time is proportional to the cell number m. Longer time will be consumed by positive problem calculation when the cell number is large. We adopt the cyclic injection method in this study. The current injection time S in this method is 105, and the number of electrodes, L, measured in this excitation method is 13, which gives a total of $105J_k$ matrices.

4. SIMULATED IMAGING OF ELECTRICAL IMPEDANCE TOMOGRAPHY IN GROUNDING GRID

In order to verify the improvement effect of the ITR-Lp algorithm for the ill conditioned inverse problem of grounding grid, this paper first considers the influence of different node distributions on the imaging results to determine the node distribution types that are relatively easy to image. Next, by constructing two different grounding grid models, one with a known topology structure and the other with an unknown topology structure, simulation studies are conducted. Lastly, to address the long detection time for large grounding grids, a block imaging based on a 2×2 grid is proposed. In this study, grounding grid models with different numbers of corrosion are established in COMSOL. Then, measurement voltage data are obtained through combined simulation using MATLAB and COMSOL. Finally, image reconstruction is performed using MATLAB to validate the effectiveness of the ITR-Lp algorithm.

4.1. The Impact of Node Distribution on Convergence

In grounding grid electrical impedance tomography imaging, the distribution of nodes is not like that in medical electrical impedance tomography imaging, where nodes are distributed around the imaged object. Instead, in grounding grid electrical impedance tomography imaging, nodes are distributed on the flat steel of the grounding grid. To investigate whether the distribution of nodes at different positions affects the imaging results, this study categorizes the nodes into three types: all boundary nodes, all interior nodes, and a combination of half boundary and half interior nodes. Simulation studies are conducted on these three types of node distributions using the ITR-

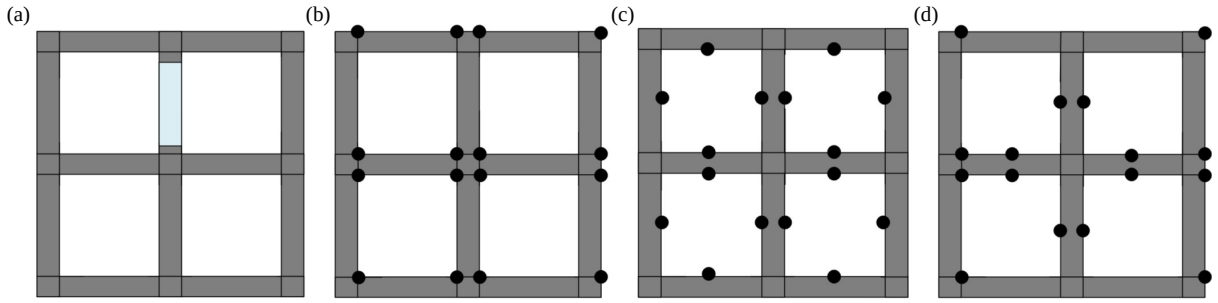

FIGURE 4. Corrosion and diagram of different node distributioon. (a) Corrosion schematic. (b) Boundary nodes. (c) Interior nodes. (d) Mixed nodes.

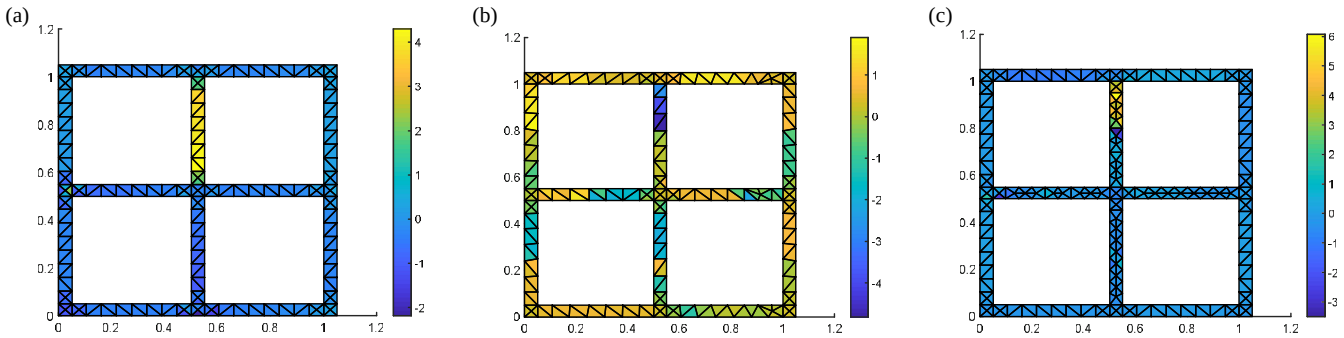

FIGURE 5. Imaging maps of different node distributions. (a) Boundary nodes. (b) Interior nodes. (c) Mixed nodes.

Lp algorithm. Figs. 4(a), (b), (c), and (d) depict the different node distribution schematics. Since most substation grounding grid structures are consistent in practice, a model with a known grounding grid structure is used for modeling and calculation. In this model, the soil and corrosion are removed, leaving only the flat steel structure of the grounding grid. Because this model only consists of flat steel and does not have severe ill-conditioning in the inverse problem compared to models with unknown topology information, the regularization parameter is obtained through multiple simulation experiments. For the improved Tikhonov regularization, the regularization parameter is determined through simulations, whereas, a value of $p = 1.5$ is chosen based on the literature for the Lp regularization parameter [32, 33], which indicates that the convergence and accuracy of Lp regularization are good when $p = 1.5$. Thus, in this study, the regularization parameter is determined to be 0.0001 under the condition of $p = 1.5$.

From Fig. 5, it can be observed that the image of the boundary nodes converges, accurately indicating the location of corrosion. However, the image of the interior nodes does not converge, making it impossible to accurately distinguish the branch where corrosion is located. The image of the mixed nodes also converges, but it only displays the corrosion on half of the branch, failing to show all the corrosion.

In order to quantitatively evaluate the quality of the reconstructed image, the relative error of resistivity is introduced to evaluate the image reconstruction. The formula of relative error of resistivity is:

$$Er = \frac{1}{N}\sum_{i=1}^{N}\frac{\rho_i^k - \rho_i}{\rho_i} \tag{22}$$

where ρ_i^k is the resistivity of the ith cell obtained from the kth iteration, ρ_i the initial resistivity of the ith cell, and N the number of finite element discretization elements in the inverse problem model.

From Fig. 6 of the iterative convergence, it can be observed that the convergence of boundary nodes is the best, while that of the central nodes is the worst. Although the convergence of mixed nodes can also show partial corrosion, its convergence is also poor. With the increase of iteration times, its imaging will also become non-convergent, unable to identify the branch where the corrosion occurs. It is known that the distribution of nodes will affect the quality and convergence of imaging. Therefore, the subsequent simulation nodes will be based on the boundary nodes with good convergence performance.

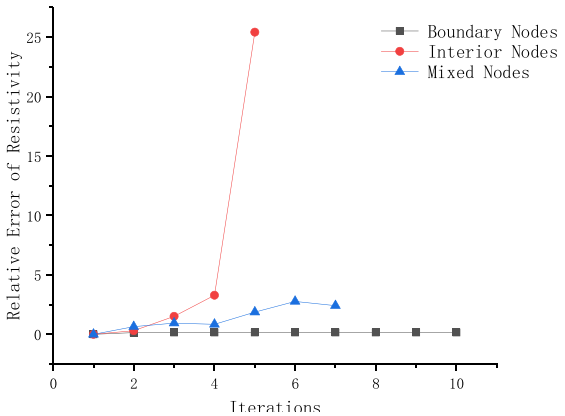

FIGURE 6. Convergence graph of different node distributions.

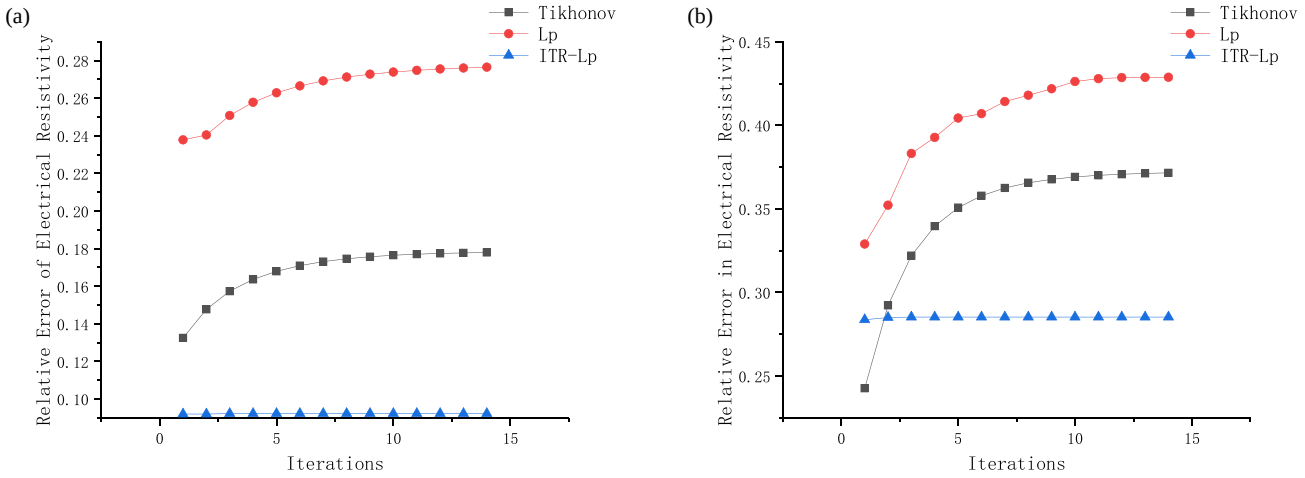

FIGURE 7. Convergence curve of iterations on 3×3 grid. (a) One corrosion. (b) Three corrosion.

4.2. Grounding Grid Model Based on Known Topology Structure

To validate the improved performance of the ITR-Lp algorithm proposed in this paper for inverse problems, four different simulation cases were considered. These cases were studied taking into account the size of the model, the number and distribution of corrosions. The forward problem model parameters for each simulation case were the same as described earlier, and the solution of their inverse problems was conducted using a model with known structure for imaging studies. The regularization parameters required for each algorithm were also the same as described earlier.

From the convergence curves of these three algorithms shown in Fig. 7 and Fig. 8, it can be observed that, compared to the other two algorithms, the ITR-Lp mixed regularization shows faster convergence speed for corrosion at locations 1 to 2, converging after 2 to 3 iterations. In contrast, the Lp regularization and Tikhonov regularization exhibit slower iteration speeds, requiring 7 or 8 iterations to converge. Therefore, the ITR-Lp mixed regularization algorithm has the fewest iterations and the lowest relative error in electrical resistivity, indicating higher imaging quality.

From Fig. 9, it can be seen that both the 3×3 grid and 4×3 grid show that the Tikhonov regularization, Lp regularization, and ITR-Lp mixed regularization can accurately display the branches where corrosion occurs as well as the number of corrosions. As shown in Table 2, the relative error in electrical resistivity computed using the ITR-Lp mixed regularization method is the lowest, indicating a good imaging effect.

TABLE 2. Relative errors of resistivity.

Grid Types	Number of Corrosions	Tikhonov	Lp	ITR-Lp
3×3	1	0.1779	0.2764	0.2764
3×3	3	0.3715	0.4287	0.2853
4×3	1	0.1334	0.2593	0.0897
4×3	3	0.2331	0.4737	0.1389

4.3. Grounding Grid Model Based on Unknown Topology Information

Due to the unknown topology structure of the grounding grid, the area to be imaged is larger, resulting in a more severe ill-posed nature of the electrical impedance tomography imaging problem. Therefore, selecting an appropriate regularization parameter is crucial for successful imaging. For the regularization parameter of the Tikhonov regularization, this paper determines it using the U-Curve method. The U-Curve method, which is a modification of the L-Curve, is used to determine the regularization parameter. The method finds the value of the regularization parameter that minimizes the error function by plotting the relationship between the error function and regularization parameter. Compared to L-Curve method, the U-Curve method is more adaptive because it dynamically selects the inflection point of the U-shaped curve as the optimal parameter according to the shape of the curve [34].

The regularization parameters for corrosion at one location and two locations are found to be 0.3662 and 0.1593, respectively, for Tikhonov regularization, as shown in the U-curve of Tikhonov regularization in Fig. 10. Regarding the selection of the Lp regularization parameters p and λ, based on previous literature, this paper chooses $p = 1.5$. For the regularization parameter λ, under the condition of $p = 1.5$, after multiple simulations, it was found that $\lambda = 0.0055$ yields good reconstruction for corrosion at one location, while $\lambda = 0.0025$ yields good reconstruction for corrosion at two locations. Fig. 11 shows the grounding grid images for corrosion at one location and two locations using the Tikhonov algorithm, Lp algorithm, and ITR-Lp algorithm.

From the imaging results in Fig. 11, it can be observed that the imaging area of Tikhonov regularization is relatively scattered and cannot accurately distinguish the boundary between soil and flat steel. The imaging area of Lp regularization is concentrated, and the contrast of the boundary is higher than that of Tikhonov regularization, but its stability is poor, leading to inaccurate solution region. The ITR-Lp mixed regularization algorithm combines the advantages of both approaches, resulting in high contrast of the boundary between soil and flat steel

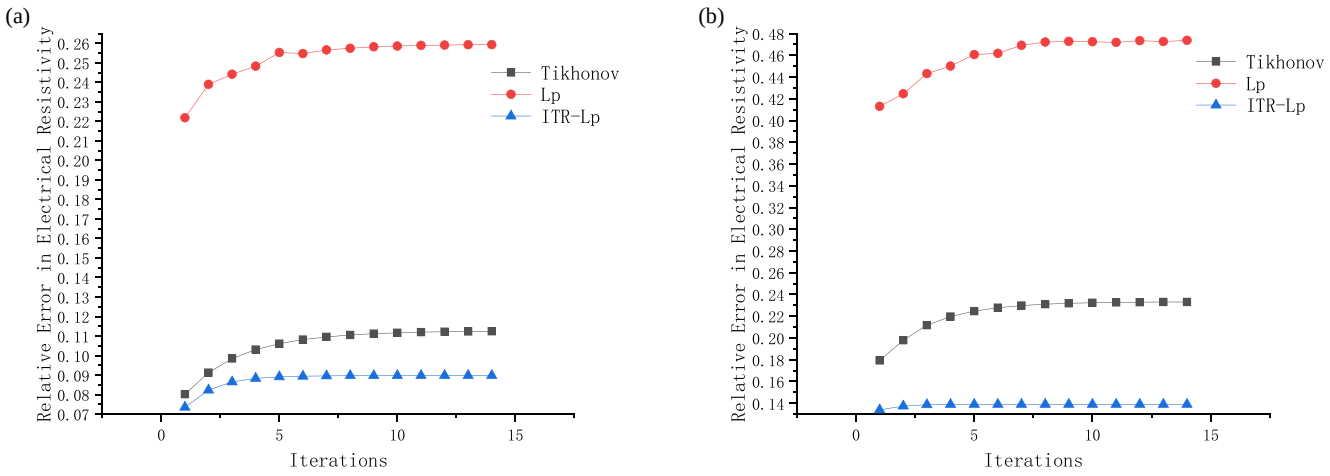

FIGURE 8. Convergence curve of iterations on 4×3 grid. (a) One corrosion. (b) Three corrosion.

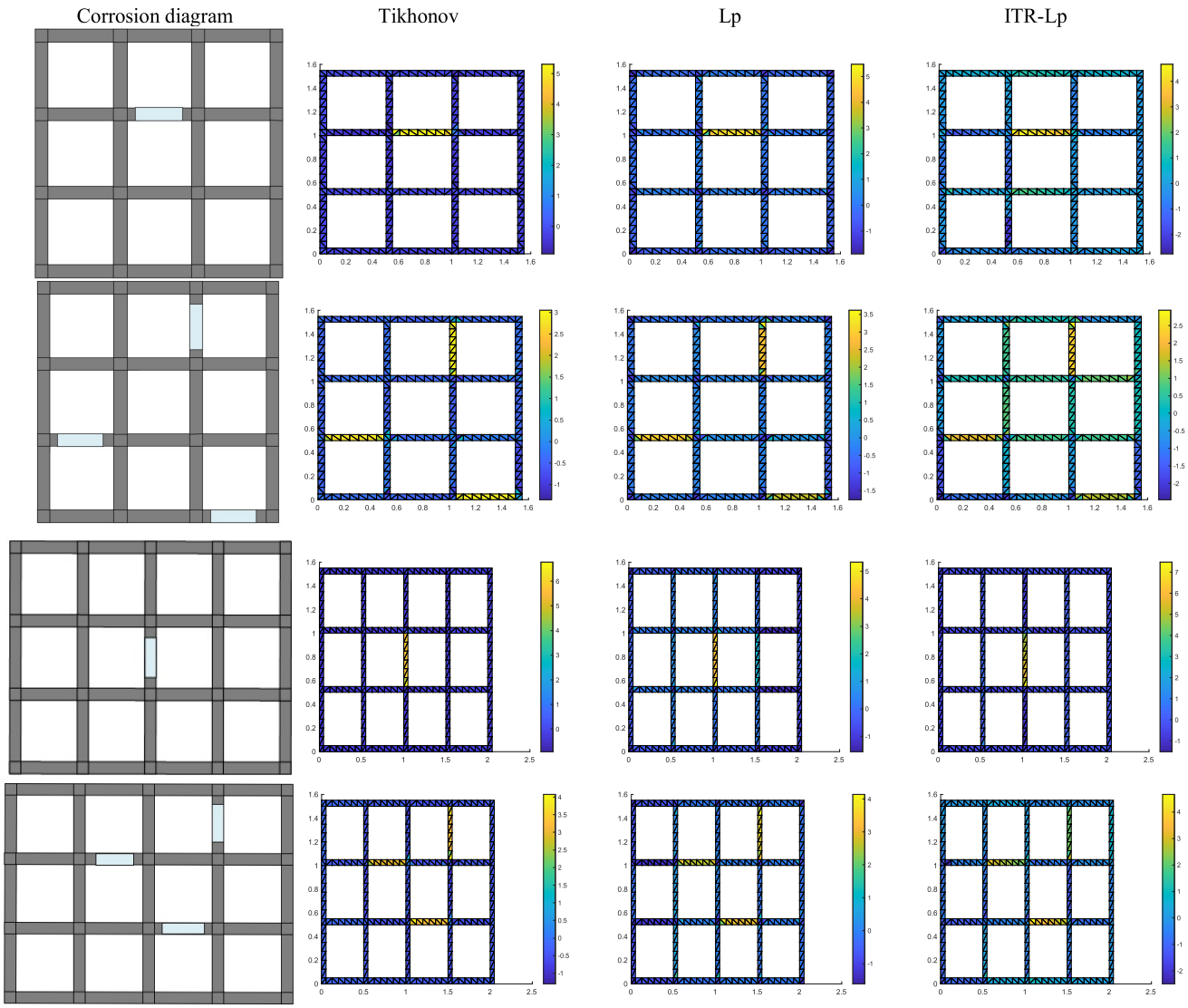

FIGURE 9. Different grid imaging images.

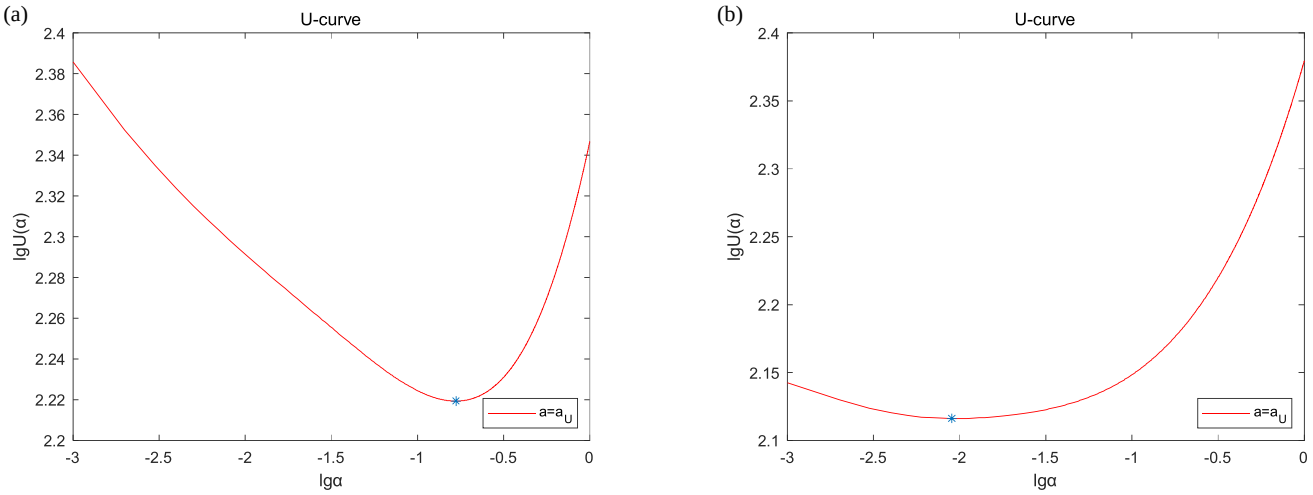

FIGURE 10. U-shaped curves with different degrees of corrosion. (a) One corrosion. (b) Two corrosions.

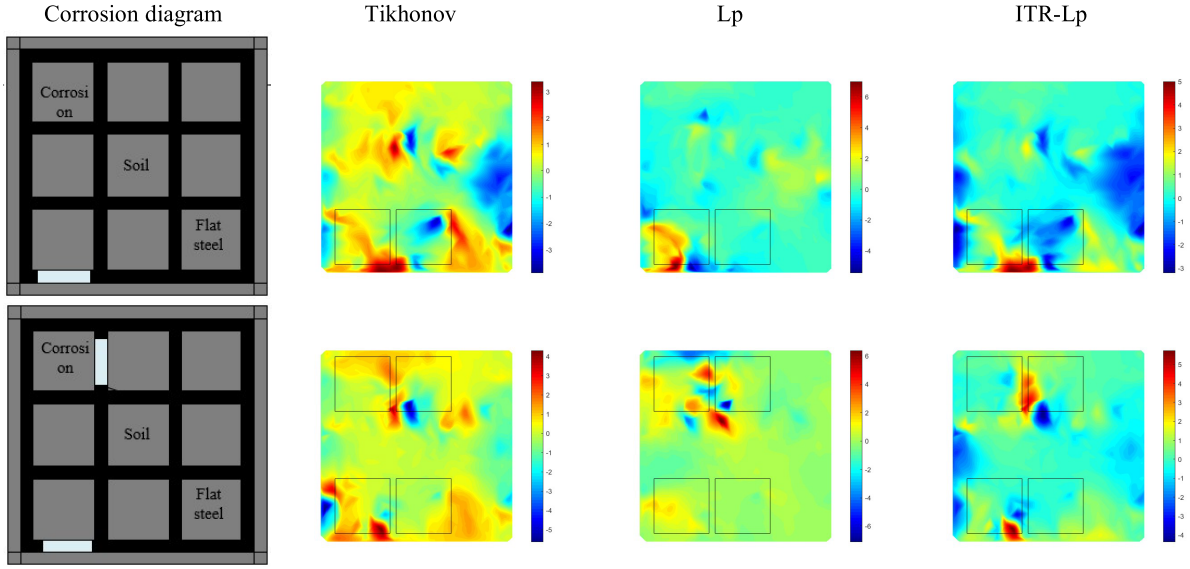

FIGURE 11. Comparison of grounding grid reconstruction images using different algorithms.

in the imaging area, and the unknown and size of the target region are well aligned with corrosion diagram.

Table 3 shows that, whether it is a single or double corrosion scenario, the ITR-Lp mixed regularization algorithm yields the smaller relative error in resistivity than the other two algorithms. The comparison results demonstrate that the proposed ITR-Lp mixed regularization algorithm improves the contrast of the boundary between soil and flat steel in the image while ensuring solution stability, and achieves better imaging quality than the other two algorithms.

TABLE 3. Relative errors of resistivity.

Type	Tikhonov	Lp	ITR-Lp
One corrosion	0.1354	0.1441	0.0168
Twe corrosions	0.1653	0.1920	0.0451

4.4. Partition Imaging Based on 2×2 Grid

In practical applications, due to the large area occupied by grounding grids, there are issues such as the computational burden and long calculation times when overall imaging is conducted using the Jacobian matrix. Therefore, the approach of partition imaging for large grounding grid is used, where the block images are combined to obtain the overall grounding grid image. Through simulation analysis, it was found that the computation time for the Jacobian matrix of a 2×2 grid is approximately 10 minutes, which is significantly lower than the 4 hours for a 3×3 grid. Additionally, most grounding grid have a mesh structure, making the selection of a 2×2 grid quite flexible. In this study, a 4×6 grid is divided into 6 regions of 2×2 grids for imaging. The voltage data from these six block regions are measured for imaging. A 4×6 grounding grid model is established in COMSOL, consisting of 766 partition elements, with dimensions of $2.05\,\text{m} \times 3.05\,\text{m}$. This model is then divided into

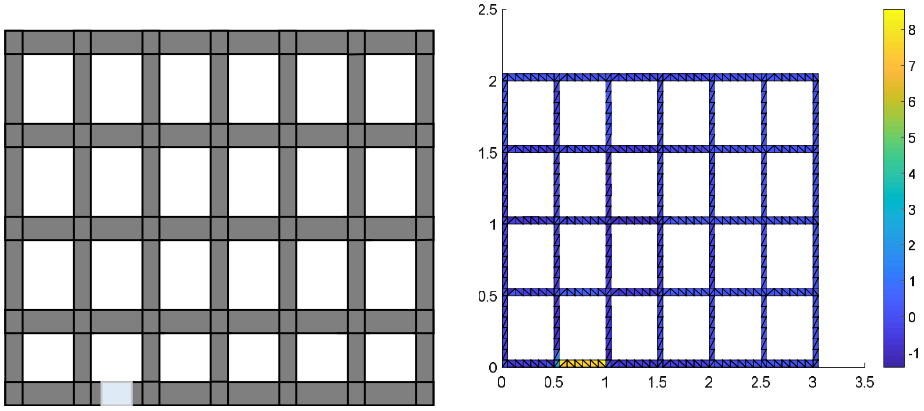

FIGURE 12. 4×6 corrosion diagram and imaging results.

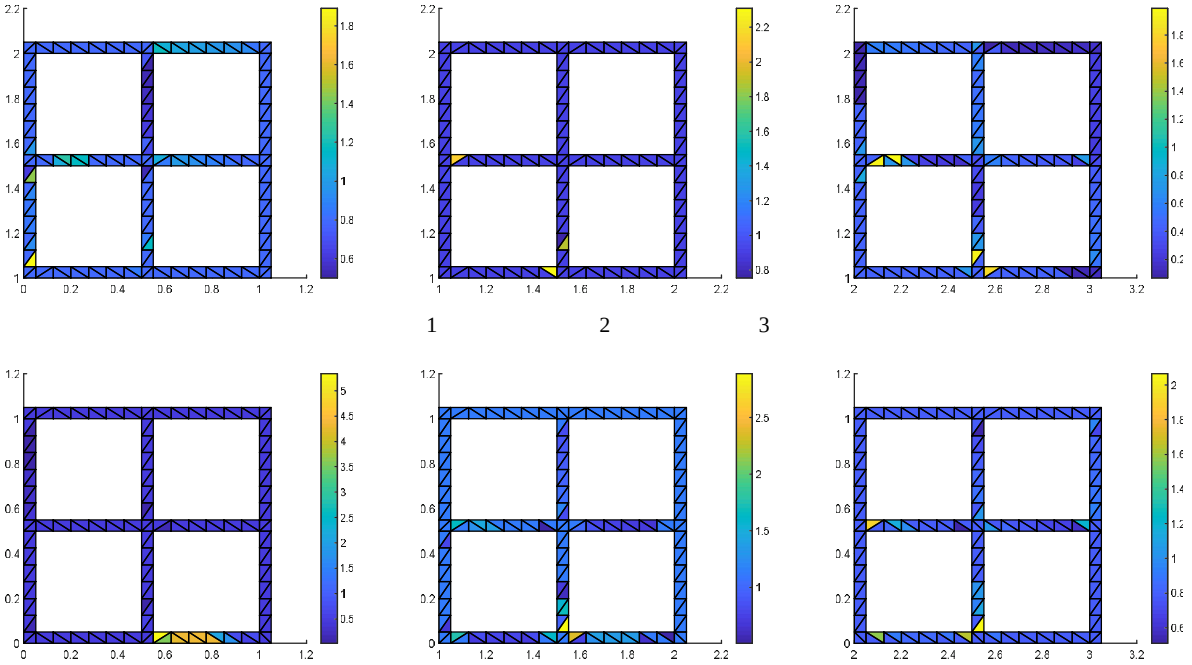

FIGURE 13. 4×6 grid separated imaging.

6 inverse problem models of 2×2 grids, each with 156 partition elements.

According to Eq. (21), the positive problem computing times of the 4×6 grid and 2×2 grid for computing the Jacobi matrix are 80535 and 16485, respectively, and the numbers of times these two types of grids do the difference operation to compute the Jacobi matrix are 1045590 and 212940, respectively, in which the size of the Jacobi matrix for 4×6 grid is 1365 rows and 766 columns, and the size of the Jacobi matrix for 2×2 grid is 1365 rows and 156 columns. From the comparison, we can see that the Jacobi matrix size of the 2×2 grid is smaller than that of the 4×6 grid in terms of the number of times of calculating the positive problem, the number of times of doing the difference operation, and the size of the Jacobi matrix.

Figures 12 and 13 correspond to the overall imaging and separated imaging of the 4×6 grid, respectively. It can be observed that for the overall imaging of the 4×6 grid, the ITR-Lp regularization can successfully display the branches where corrosion occurs, validating the effectiveness of the algorithm. From the fourth part of Fig. 13, it can be seen that the block imaging method displays the branches where corrosion occurs, which can be used for diagnosing corrosion in the grounding grid. The time taken to compute the Jacobian matrix for these two methods is shown in Table 4. All simulations were performed on a computer with an R5 CPU (3.30 GHz) and 16 GB RAM configuration, using MATLAB for computation. As shown in Table 4, the time taken for separated imaging is much less than that for overall imaging. This indicates that the block imaging method can shorten the detection time and can also be used to individually detect specific regions of interest in the grounding grid, without the need for overall imaging, thereby improving detection efficiency.

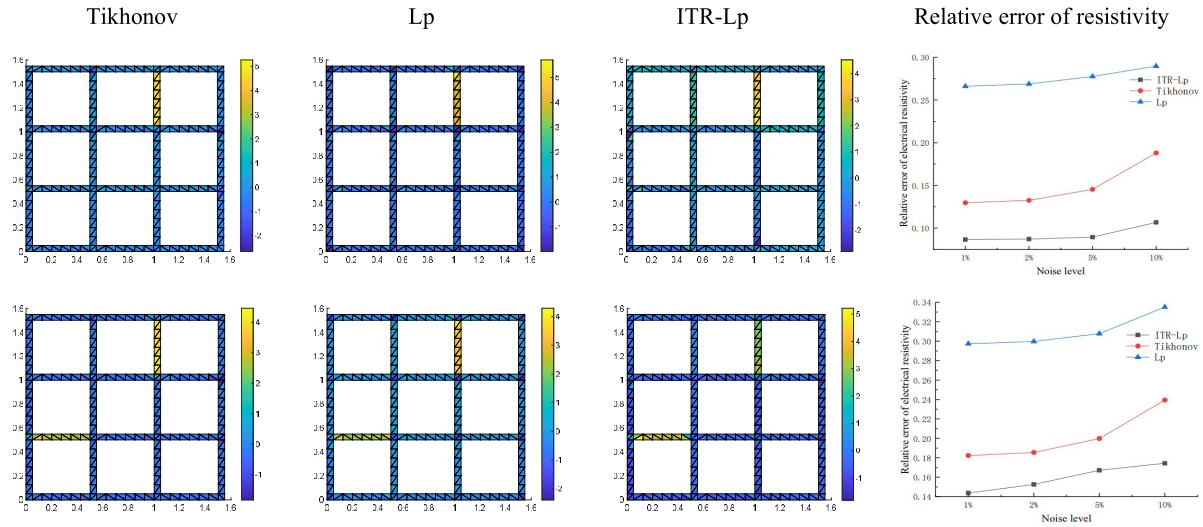

FIGURE 14. 3×3 grid imaging in 10% noise and relative error of resistivity.

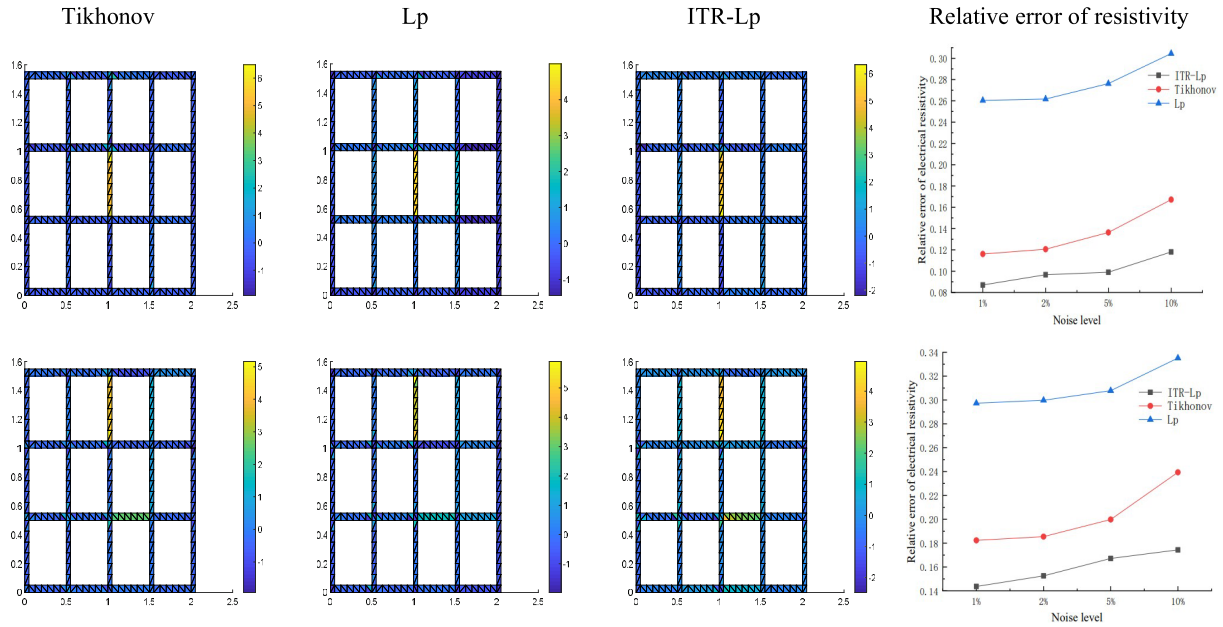

FIGURE 15. 3×3 grid imaging in 10% noise and relative error of resistivity.

TABLE 4. Time for calculating Jacobian matrix.

way	time (min)
Overall Imaging	1503
separated imaging	60

4.5. The Effect of Different Measurement Noises

In practical applications, measurement noise is inevitable due to the insufficient measurement performance of the measurement equipment or the interference of environmental factors, so the measurement noise of the measurement data has a certain impact on the reconstruction of the inverse problem. In order to test the anti-noise performance of the method proposed in this paper, based on the 3×3 grid and 4×3 grid models constructed in Section 4.2, the corrosion location and the number of corrosions are reset, and cyclic measurements are made to get the voltage data of the new model, and add different degrees of Gaussian noise to the measurement data of the grounding grid model, which is used to simulate the noise in the actual measurement process, so Gaussian noise with a mean value of 0, and standard deviation of 1%, 2%, 5%, and 10% is added to the data of each model. Figs. 14 and 15 show the reconstruction of the grounding grid model after adding 10% Gaussian white noise and relative resistivity error for different noise levels.

By comparing the reconstructed maps of grounding grids with 10% Gaussian white noise, we observe that both Tikhonov regularization and ITR-Lp regularization accurately depict the locations of corrosion branches, regardless of whether it is a 3×3 grid or a 4×3 grid. However, for the 4×3 grid with

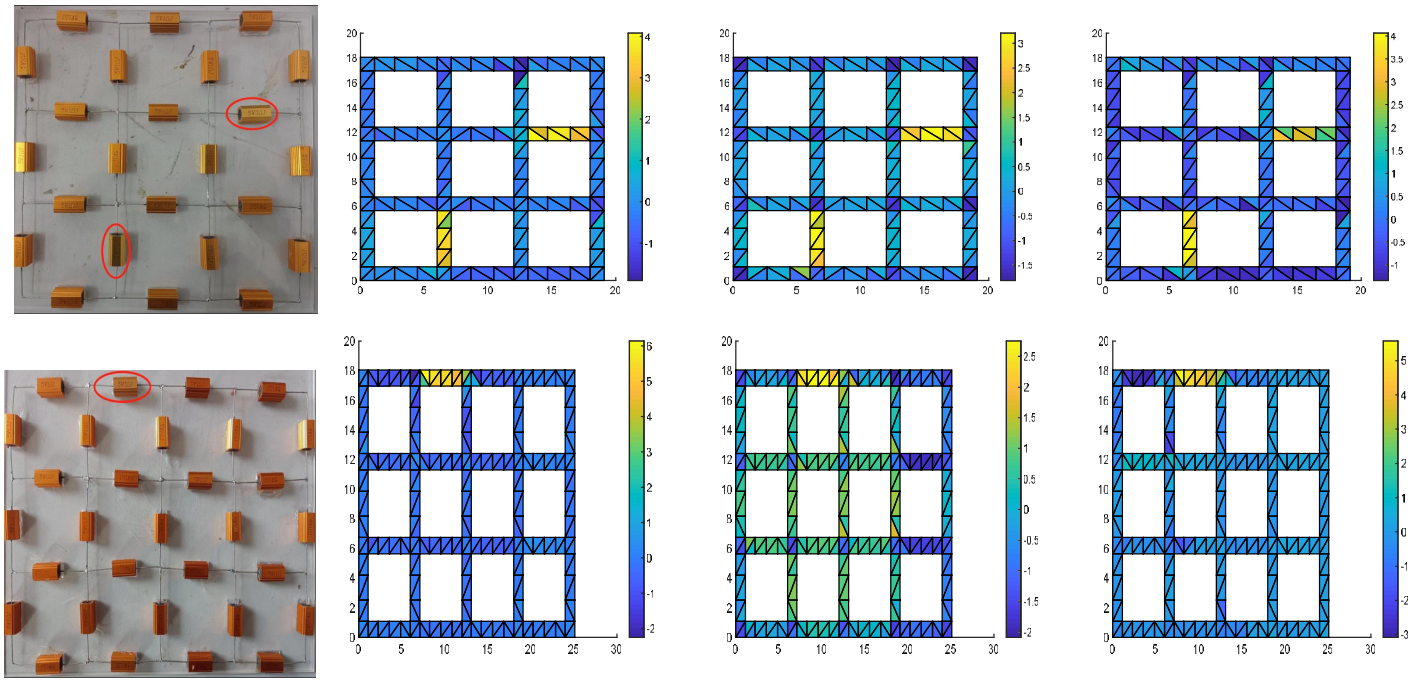

FIGURE 16. Experimental imaging of resistor network.

two instances of corrosion, Lp regularization is significantly affected by noise, resulting in smaller differences between the second corroded branch and the normal branches. All three regularization algorithms are influenced by measurement noise, and as the noise level increases, the relative errors in the reconstructed resistivity images increase, leading to lower image quality. Comparing the imaging quality of the three algorithms at the same noise level, we find that the ITR-Lp regularization algorithm exhibits the lowest relative error in resistivity imaging, followed by Tikhonov regularization, while Lp regularization produces the largest reconstruction image errors. The simulation results indicate that the proposed ITR-Lp regularization algorithm demonstrates greater robustness to noise than Tikhonov regularization and Lp regularization algorithms. Since the topological structure of the grounding grid model is known, the ill-conditioning of the grounding grid inverse problem is relatively mild. Therefore, the parameters of these three regularization algorithms were determined through a large number of simulations, with specific values given in Table 5.

TABLE 5. Value of regularization parameter.

Type	Tikhonov	Lp	ITR-Lp
3×3 grid 1 corrosion	$\alpha = 0.1$	$p = 1.5$ $\lambda = 0.001$	$\alpha = 0.1$ $p = 1.5$ $\lambda = 0.0001$
3×3 grid 2 corrosion	$\alpha = 0.1$	$p = 1.5$ $\lambda = 0.001$	$\alpha = 0.1$ $p = 1.5$ $\lambda = 0.0001$
4×3 grid 1 corrosion	$\alpha = 0.1$	$p = 1.5$ $\lambda = 0.001$	$\alpha = 0.1$ $p = 1.5$ $\lambda = 0.00001$
4×3 grid 2 corrosion	$\alpha = 0.1$	$p = 1.5$ $\lambda = 0.0001$	$\alpha = 0.1$ $p = 1.5$ $\lambda = 0.0001$

5. GROUNDING GRID SIMULATION EXPERIMENT

5.1. Simulated Grounding Grid Test

In this section, we conducted experiments on corrosion diagnosis of both a resistor network and a simulated grounding grid. A 3×3 and a 4×3 resistor network were constructed to simulate the grounding grid, where a $1\,\Omega$ resistor represented the branch of the normal flat steel in the grounding grid, and a $3\,\Omega$ resistor represented the branch of corroded flat steel. A simulated grounding grid was also constructed by welding galvanized flat steel with a cross section of $50\,\text{mm} \times 5\,\text{mm}$ into a 4×6 grid, where the length of the flat steel was 50 cm. The flat steel was cut off by 2 mm at the corroded location, and a 10 cm long flat steel was tied to the cut-off position with insulating tape to simulate the corrosion scenario. The corrosion branch presents a higher resistance value than healthy branches as corrosion leads to oxidation of the metal surface and formation of corrosive substances which increase the obstruction to the passage of current, therefore increasing the resistance of the branch, whereas a branch circuit without corrosion is not affected by these and hence has a lower resistance value. In this experiment, galvanized flat steel pieces of 50 cm in length were adopted. The measured resistance of the flat steel was $2.623\,\text{m}\Omega$, and the measured resistance of the simulated corroded branch was $4.346\,\text{m}\Omega$. The ratio of the resistance values was $1.656 : 1$, which satisfies the requirements for corrosion imaging. The corroded position was marked with a red circle.

Figure 16 shows the experimental image of resistance network imaging. Fig. 17 shows the 16-electrode grounding grid imaging experimental platform, including 16 detection electrodes, data acquisition board, main control chip, constant current source, flat steel model, and the upper computer. Table 6

TABLE 6. Value of regularization parameter.

Type	Tikhonov	Lp	ITR-Lp
3×3 resistance	$\alpha = 0.1$	$p = 1.5$ $\lambda = 0.0001$	$\alpha = 0.1$ $p = 1.5$ $\lambda = 0.0001$
4×3 resistance	$\alpha = 0.1$	$p = 1.5$ $\lambda = 0.001$	$\alpha = 0.1$ $p = 1.5$ $\lambda = 0.0001$
4×6 flat steel	$\alpha = 0.1$	$p = 1.5$ $\lambda = 0.00025$	$\alpha = 0.1$ $p = 1.5$ $\lambda = 0.0001$

TABLE 7. Relative errors of resistivity.

Type	Tikhonov	Lp	ITR-Lp
3×3 resistance	0.2241	0.3774	0.1935
4×3 resistance	0.1178	0.3210	0.1089
4×6 flat steel	0.2874	0.3668	0.2434

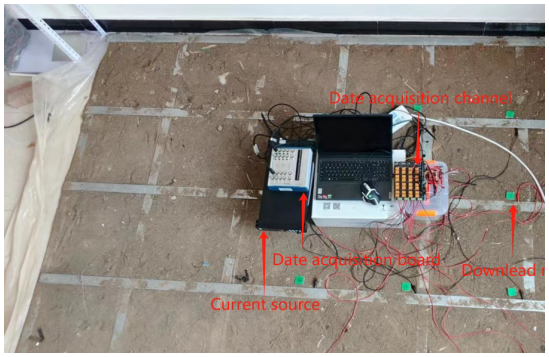

FIGURE 17. Grounding grid imaging platform.

way	time (min)
Overall Imaging	425
separated imaging	43

TABLE 8. Time for calculating Jacobian matrix.

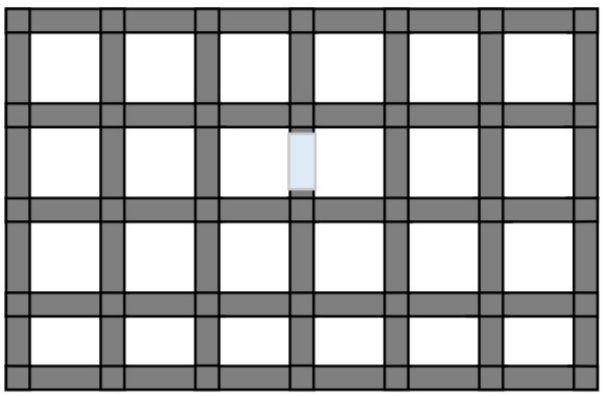

Corrosion Diagram

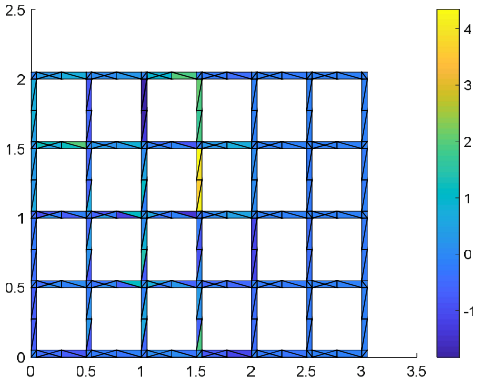

Tikhonov

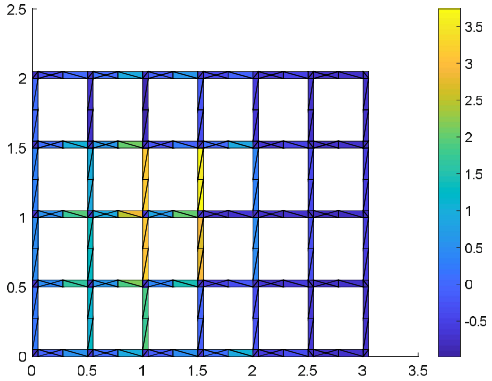

Lp

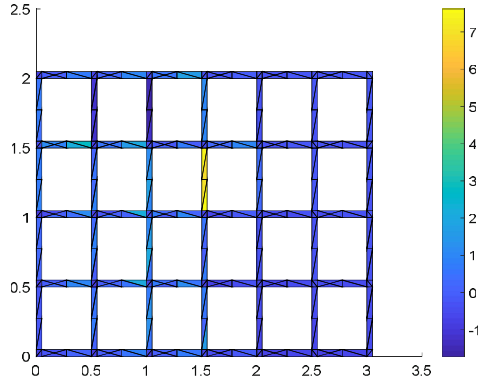

ITR-Lp

FIGURE 18. Experimental imaging of simulated grounding grid.

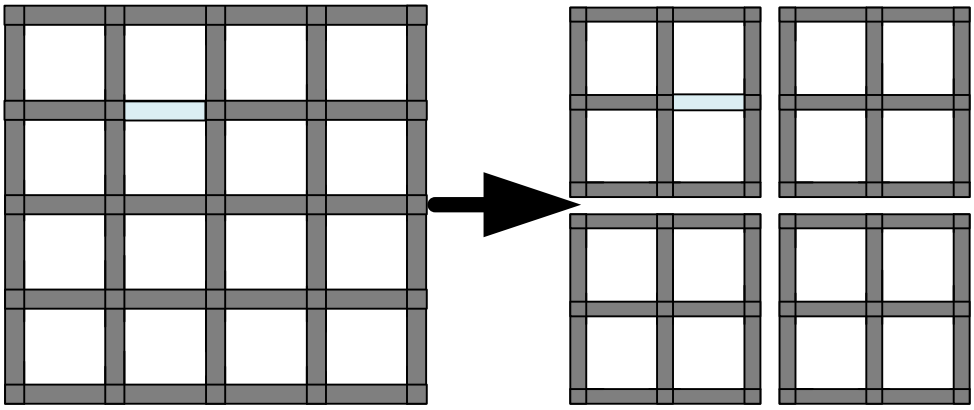

FIGURE 19. Block diagram of resistance network.

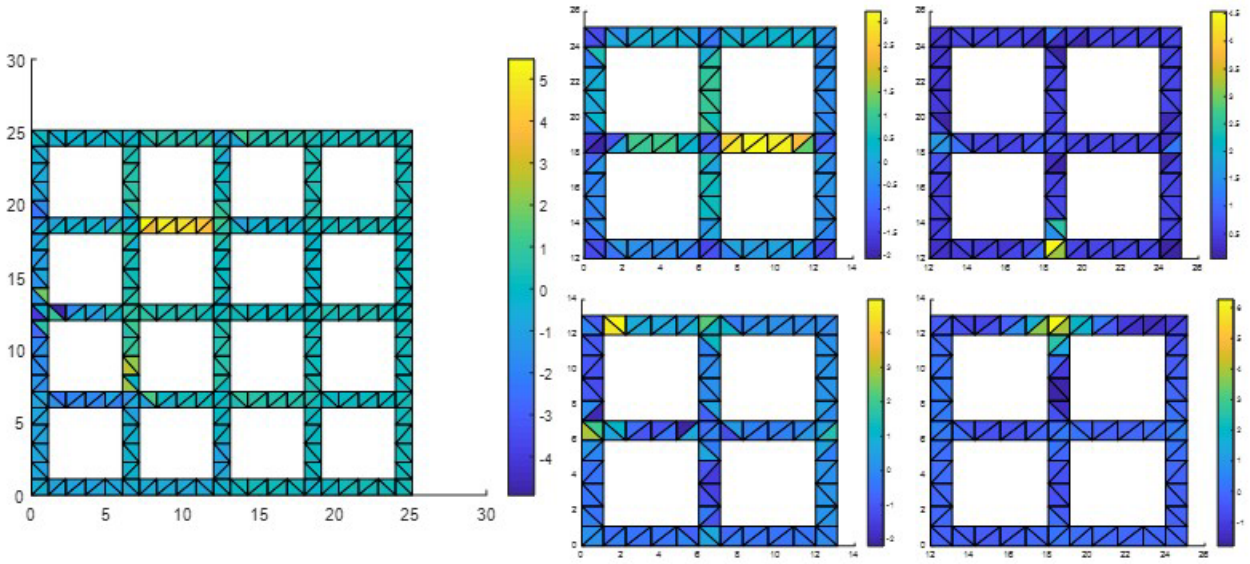

FIGURE 20. Comparison of overall imaging map and sub-regional imaging map.

shows the regularization parameters used in the imaging experiment.

From the imaging results of the experimental diagrams, it can be observed that for both the resistor network experiment and simulated grounding grid experiment, all three regularization algorithms can accurately display the branch where corrosion occurred. However, compared with the other two algorithms, the imaging quality of the Lp regularization algorithm is inferior. The ITR-Lp mixed regularization algorithm proposed in this paper has the less relative error in electrical resistivity and higher imaging quality than the other two regularization algorithms. The experimental results are consistent with the simulation results.

5.2. Subregion Imaging Experiment

To validate the feasibility of the subregion imaging method, a 4×4 resistive network model is constructed to simulate the grounding network for the partition imaging experiments. The resistive network is established with a corrosion branch, and the 4×4 resistive network model is partitioned with a 2×2 grid to split the whole large imaging region into four small imaging regions. In the partition imaging experiments, the main comparison in the subregion imaging experiments is the time to compute the Jacobi matrix, so the environment to run the MATLAB imaging program is kept the same, and all computations are carried out on a computer with an R5 CPU (3.30 GHz) and 16 GB RAM. The overall and subregion imaging maps are shown in Fig. 18. Table 7 shows a comparison of the time consumed by these two methods to solve the Jacobi matrix. The block diagram of resistance networks is shown in Fig. 19. Table 8 shows that the total time taken to calculate the Jacobian matrix for the four 2×2 grids in the subregion imaging method is only 43 minutes, which is approximately one-tenth of the time consumed by the overall imaging method. The proposed method significantly reduces the time required for imaging. As shown in Fig. 20, the proposed method accurately displays the position and quantity of the corroded branches.

6. CONCLUSION

This paper proposes the ITR-Lp hybrid regularization algorithm to address the ill-posed nature of the impedance imaging inverse problem in grounding grid. Firstly, study the impact of node distribution on imaging quality and select nodes with high imaging quality distribution. Secondly, through theoretical analysis and simulation verification, it has been proven that this method improves the convergence of the solution by introducing a correction matrix with different correction amplitudes for different singular values, effectively reducing the ill-conditioning in the reconstruction process of the grounding grid inverse problem. This method obtains solutions with lower sparsity through Lp regularization, improves the boundary contrast of the reconstructed image, and obtains high-quality reconstructed images. The final experimental results show that the ITR-Lp hybrid regularization algorithm has lower relative resistivity error and higher edge contrast, which better reduces the ill posed nature of electrical impedance imaging tomography inverse problems.

ACKNOWLEDGEMENT

This work was supported by the Liaoning Provincial Department of Science and Technology for general projects 2021-MS-338.

REFERENCES

[1] Fu, Z., X. Wang, Q. Wang, X. Xu, N. Fu, and S. Qin, "Advances and challenges of corrosion and topology detection of grounding grid," *Applied Sciences*, Vol. 9, No. 11, 2290, 2019.

[2] Zhang, C., Y. Liao, X. Gao, J. Zhao, Y. Yuan, and R. Liao, "Research advances of soil corrosion of grounding grids," *Micromachines*, Vol. 12, No. 5, 513, 2021.

[3] Alam, A. K. M. M., M. Kandic, D. J. Thomson, and G. E. Bridges, "Rod insertion TDR for detecting corrosion damage in vertical grounding electrodes," *IEEE Transactions on Power Delivery*, Vol. 38, No. 2, 1230–1238, 2023.

[4] Yu, C., Z. Fu, Q. Wang, H.-M. Tai, and S. Qin, "A novel method for fault diagnosis of grounding grids," *IEEE Transactions on Industry Applications*, Vol. 51, No. 6, 5182–5188, 2015.

[5] Lu, C., T. Zhang, S. Sun, Z. Cao, M. Xin, G. Fu, T. Wang, and X. Wang, "Fault diagnosis of tower grounding conductor based on the electromagnetic measurement and neural network," *IEEE Transactions on Instrumentation and Measurement*, Vol. 71, 1–9, 2022.

[6] Liang, G., S. Ren, S. Zhao, and F. Dong, "A Lagrange-Newton method for EIT/UT dual-modality image reconstruction," *Sensors*, Vol. 19, No. 9, 1966, 2019.

[7] Liu, S., H. Wu, Y. Huang, Y. Yang, and J. Jia, "Accelerated structure-aware sparse Bayesian learning for three-dimensional electrical impedance tomography," *IEEE Transactions on Industrial Informatics*, Vol. 15, No. 9, 5033–5041, 2019.

[8] Wang, X., Z. Fu, Y. Wang, R. Liu, and L. Chen, "A nondestructive testing method for fault detection of substation grounding grids," *Sensors*, Vol. 19, No. 9, 2046, 2019.

[9] Liu, K., F. Yang, S. Zhang, L. Zhu, J. Hu, X. Wang, and U. Irfan, "Research on grounding grids imaging reconstruction based on magnetic detection electrical impedance tomography," *IEEE Transactions on Magnetics*, Vol. 54, No. 3, 1–4, 2018.

[10] Yang, F., Y. Wang, M. Dong, X. Kou, D. Yao, X. Li, B. Gao, and I. Ullah, "A cycle voltage measurement method and application in grounding grids fault location," *Energies*, Vol. 10, No. 11, 1929, 2017.

[11] Li, X., F. Yang, J. Ming, A. Jadoon, and S. Han, "Imaging the corrosion in grounding grid branch with inner-source electrical impedance tomography," *Energies*, Vol. 11, No. 7, 1739, 2018.

[12] Chen, Y., Y. Xiang, Z. Shi, J. Lu, and Y. Wang, "Tikhonov regularized penalty matrix construction method based on the magnitude of singular values and its application in near-field acoustic holography," *Mechanical Systems and Signal Processing*, Vol. 170, 108870, 2022.

[13] Chen, Y. and H. Yan, "Reconstruction of complex temperature field based on improved Tikhonov regularization," in *Journal of Physics: Conference Series*, Vol. 1754, No. 1, 012207, IOP Publishing, 2021.

[14] Dimas, C., N. Uzunoglu, and P. P. Sotiriadis, "An efficient point-matching method-of-moments for 2D and 3D electrical impedance tomography using radial basis functions," *IEEE Transactions on Biomedical Engineering*, Vol. 69, No. 2, 783–794, 2021.

[15] Estatico, C., M. Pastorino, and A. Randazzo, "A novel microwave imaging approach based on regularization in Lp Banach spaces," *IEEE Transactions on Antennas and Propagation*, Vol. 60, No. 7, 3373–3381, 2012.

[16] Zhang, L., G. Xu, Q. Xue, H. Wang, and Y. Xu, "An iterative thresholding algorithm for the inverse problem of electrical resistance tomography," *Flow Measurement and Instrumentation*, Vol. 33, 244–250, 2013.

[17] Liu, X. and Z. Liu, "A novel algorithm based on L1-Lp norm for inverse problem of electromagnetic tomography," *Flow Measurement and Instrumentation*, Vol. 65, 318–326, 2019.

[18] Li, J., S. Yue, M. Ding, Z. Cui, and H. Wang, "Adaptive lp regularization for electrical impedance tomography," *IEEE Sensors Journal*, Vol. 19, No. 24, 12 297–12 305, 2019.

[19] Zhu, W., "Image denoising using Lp-norm of mean curvature of image surface," *Journal of Scientific Computing*, Vol. 83, No. 2, 32, 2020.

[20] Hua, P., E. J. Woo, J. G. Webster, and W. J. Tompkins, "Finite element modeling of electrode-skin contact impedance in electrical impedance tomography," *IEEE Transactions on Biomedical Engineering*, Vol. 40, No. 4, 335–343, 1993.

[21] Zhang, X., G. Xu, S. Zhang, Y. Li, Y. Guo, Y. Li, Y. Wang, and W. Yan, "A numerical computation forward problem model of electrical impedance tomography based on generalized finite element method," *IEEE Transactions on Magnetics*, Vol. 50, No. 2, 1045–1048, 2014.

[22] Shi, Y., Z. Rao, C. Wang, Y. Fan, X. Zhang, and M. Wang, "Total variation regularization based on iteratively reweighted least-squares method for electrical resistance tomography," *IEEE Transactions on Instrumentation and Measurement*, Vol. 69, No. 6, 3576–3586, 2019.

[23] Song, Y., Y. Wang, and D. Liu, "A nonlinear weighted anisotropic total variation regularization for electrical impedance tomography," *IEEE Transactions on Instrumentation and Measurement*, Vol. 71, 1–13, 2022.

[24] Cheney, M., D. Isaacson, J. C. Newell, S. Simske, and J. Goble, "NOSER: An algorithm for solving the inverse conductivity problem," *International Journal of Imaging Systems and Technology*, Vol. 2, No. 2, 66–75, 1990.

[25] Cheng, W., Y. Lu, and Z. Zhang, "Tikhonov regularization-based operational transfer path analysis," *Mechanical Systems and Signal Processing*, Vol. 75, 494–514, 2016.

[26] Zong, Z., Y. Wang, S. He, and Z. Wei, "Adaptively regularized bases-expansion subspace optimization methods for electrical impedance tomography," *IEEE Transactions on Biomedical Engineering*, Vol. 69, No. 10, 3098–3108, 2022.

[27] Ramlau, R. and E. Resmerita, "Convergence rates for regularization with sparsity constraints," *Electronic Transactions on Numerical Analysis*, Vol. 37, 87–104, 2010.

[28] Engl, H. W., M. Hanke, and A. Neubauer, *Regularization of Inverse Problems*, Springer Science & Business Media, 1996.

[29] Wang, Z., Y. Xu, Y. Pei, and F. Dong, "A method of spatially adaptive Lp regularization for electrical tomography," in *2017 IEEE International Instrumentation and Measurement Technology Conference (I2MTC)*, 1–6, IEEE, 2017.

[30] Zhao, J., Y. Xu, and F. Dong, "An Lq–Lp optimization framework for image reconstruction of electrical resistance tomography," *Measurement Science and Technology*, Vol. 25, No. 12, 125402, 2014.

[31] Hu, J.-Y., J.-G. Hu, D.-L. Lan, J.-L. Ming, Y.-T. Zhou, and Y.-W. Li, "Corrosion evaluation of the grounding grid in transformer substation using electrical impedance tomography technology," in *IECON 2017 — 43rd Annual Conference of the IEEE Industrial Electronics Society*, 5033–5038, IEEE, 2017.

[32] Li, C.-N., Y.-H. Shao, W.-J. Chen, Z. Wang, and N.-Y. Deng, "Generalized two-dimensional linear discriminant analysis with regularization," *Neural Networks*, Vol. 142, 73–91, 2021.

[33] Sabett, C., A. Hafftka, K. Sexton, and R. G. Spencer, "L1, Lp, L2, and elastic net penalties for regularization of Gaussian component distributions in magnetic resonance relaxometry," *Concepts in Magnetic Resonance Part A*, Vol. 46, No. 2, e21427, 2017.

[34] Chen, M., H. Su, Y. Zhou, C. Cai, D. Zhang, and J. Luo, "Automatic selection of regularization parameters for dynamic fluorescence molecular tomography: A comparison of L-curve and U-curve methods," *Biomedical Optics Express*, Vol. 7, No. 12, 5021–5041, 2016.